Robotica (2017) volume 35, pp. 1598–1615. © Cambridge University Press 2016
doi:10.1017/S0263574716000333

Robot-assisted perception augmentation for online detection of insertion failure during cochlear implant surgery

J. Pile†, G. B. Wanna‡ and N. Simaan†‡*

†*Department of Mechanical Engineering, Vanderbilt University, Nashville, TN 37235 USA. E-mail: jason.pile@vanderbilt.edu*
‡*Department of Otolaryngology Head & Neck Surgery, Vanderbilt University, Nashville, TN 37235 USA. E-mail: george.wanna@vanderbilt.edu*

(Accepted May 2, 2016. First published online: June 9, 2016)

SUMMARY
During the past decade, robotics for cochlear implant electrode array insertion has been limited to manipulation assistance. Going beyond manipulation assistance, this paper presents the new concept of *perception augmentation* to detect and warn against the *onset* of intracochlear electrode array tip folding. This *online* failure detection method uses a combination of intraoperative electrode insertion force data and a predictive model of insertion force profile progression as a function of insertion depth. The predictive model uses statistical characterization of insertion force profiles during normal robotic electrode array insertions as well as the history of intra-operative insertion forces. Online detection of onset of tip folding is achieved using the predictive model as an input into a support vector machine classifier. Results show that the detection of tip folding onset can be achieved with an accuracy of 88% despite the use of intra-operative insertion force data representing incomplete insertion. This result is significant because it allows the surgeon or robot to choose a corrective action for preventing intra-cochlear complications.
KEYWORDS: cochlear implants, fault detection, medical robotics.

1. Introduction

Cochlear implants (CI) (Fig. 1) restore auditory perception in patients with sensorineural hearing loss. These prothesis are typically a two part system with an externally worn microphone/audio processor and an implanted electrode array in the cochlea which is positioned within close proximity to the auditory nerve. The electrode array is inserted into the scala tympani (ST) (one of three helical chambers within the cochlea). Hearing sensation is restored by using the electrodes to provide direct electrical stimulation to the auditory nerve–thereby bypassing dysfunctional hair cells which, in normal anatomy, are responsible for transduction of acoustic energy into electric stimulation of the auditory nerve.

Previous works on robot-assisted CI insertion were motivated by the need for avoiding intracochlear trauma (as further explained in the background and motivation section). Zhang et al. first introduced the concept of robotic insertion and steerable CI electrode arrays in ref. [38, 40] where different kinematic arrangements and degrees of freedom in manipulating electrode arrays during the insertion process were considered. The electrode insertion and steering path planning strategy of ref. [38] was subsequently adapted to steer perimodiolar electrode arrays (PEA).[23–26] In addition, other works (e.g. Refs. [19, 31]) presented clinically adapted versions of electrode array insertion tools.

Past works on electrode array insertion have focused on *manipulation augmentation* to enable accurate steering and insertion of electrode arrays into the narrow and delicate anatomy of the scala-tympani. Because of the hypothesis that large insertion forces are associated with a higher risk of

* Corresponding author. E-mail: nabil.simaan@vanderbilt.edu

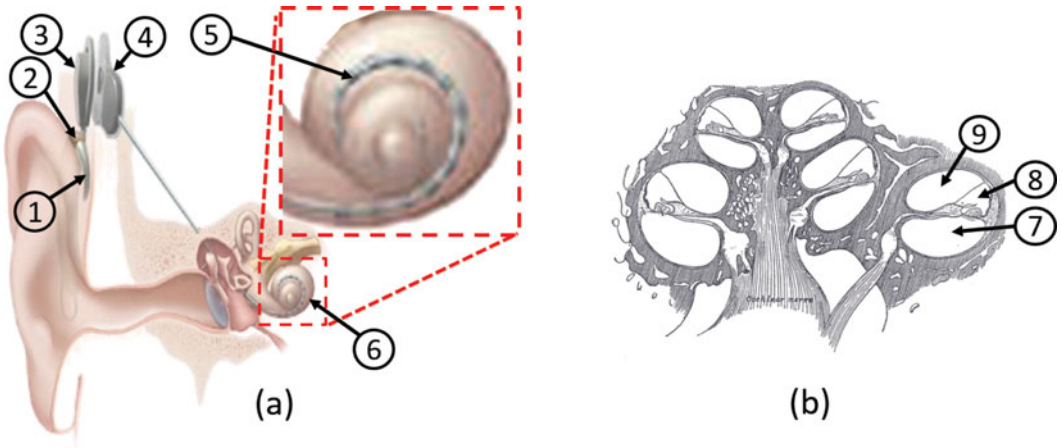

Fig. 1. (a) A cochlear implant system:[21] ① microphone,② processor, ③ transmitter, ④ reciever, ⑤ electrode array, (b) cross section of the cochlea showing ⑥ cochlea, ⑦ scala-tympani, ⑧ scala-media, ⑨ scala vestibuli.

intracochlear trauma, many works developed and used means for force sensing.[17,20,23,25,28,31,33,37,40] Surprisingly, the use force sensing information has been limited to using force data as a metric for post-evaluation of insertion quality.

In contrast to prior works limited to manipulation augmentation, this paper presents a contribution by putting forward the notion of *perception augmentation* by which the robot augments the surgeon's perception by using sensory data and inference to perceive and guard against impending undesirable insertion conditions. According to our new approach, force sensing data can be used to help surgeons extend their perception abilities by providing them with a means for *online detection* of onset of erroneous electrode insertion conditions. To the best of our knowledge, no prior works have presented the concept of perception augmentation for assisting in the monitoring of the electrode array insertion process. In-vivo force measurements were used in ref. [26] to facilitate electrode array insertion despite errors in the registration of the robot to the anatomy. This work aims to extend the concept of using intra-operative measurements to improve outcomes. Instead of focusing on using the sensory information for control action as in ref. [26], we focus on using sensory information as a means to derive inference regarding the normal progression of the insertion process.

While there are several known erroneous electrode insertion conditions (e.g. extra-cochlear buckling, intra-cochlear scalar crossing) this paper chooses to demonstrate the concept of perception augmentation for detecting the onset of tip fold-over. This erroneous condition can arise from incorrect electrode insertion technique causing the tip of the electrode array to fold over itself as insertion progresses. When tip fold-over occurs further advancement of the electrode array into the ST can cause damage to the electrode array and the intracochlear anatomy.

In our preliminary work,[25] we presented an investigation of tip fold over using support vector machine classifiers. This approach demonstrated an 89% success rate in classification of tip folding based on data collected during the *entire* insertion process (i.e. classification was done post insertion) and guided selection of appropriate feature vectors. However, during surgical insertion one is interested in detection of the *onset* of tip fold over in order to warn against a potentially harmful insertion or in order to guide corrective action during robotic insertion. This work extends[25] by investigating methods for detecting onset of tip fold-over. This effort is motivated by the desire to reduce the risk of intra-cochlear trauma.

The remainder of this paper is organized as the following: Section 2 presents background on CI surgery and motivation for this work, Section 3 presents the kinematic model used to describe PEA insertion and insertion forces. Section 4 details the experimental protocol. Section 5 proposes an algorithm for using force information to detect the onset of abnormal insertion events. Finally, Section 6 presents the results of the proposed algorithm with discussion of its meaning and limitations and Section 7 summarizes the findings.

https://doi.org/10.1017/S0263574716000333 Published online by Cambridge University Press

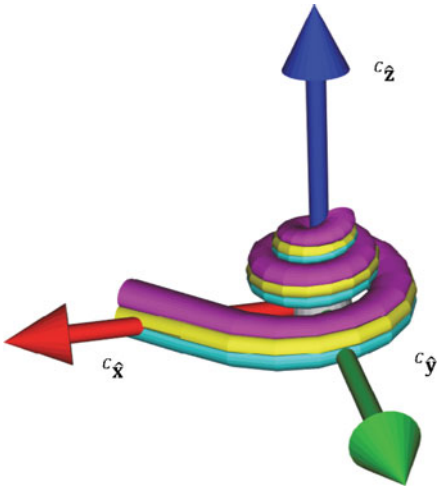

Fig. 2. Coordinate Frames and vectors describing electrode array insertion kinematics with a parametric rendering of the cochlea helical geometry and the standard cochlea coordinate frame.

2. Background and Motivation

The cochlea is a helical structure with three principal chambers; the scala vestibuli (SV), the scala media (SM), and the ST, Fig. 1(b). Most electrode arrays are designed to be inserted into the ST due to evidence that CI placement entirely in the ST results in improved hearing outcome.[13,34,35] This is attributed to the relatively larger size of the ST in comparison to the SV.

Traditionally, the cochlea is accessed by performing a mastoidectomy and exposing the facial recess.[10] The electrode array is inserted into the ST chamber of the cochlea. Entry into the ST is typically through the round window membrane or through an anterior-inferior cochleostomy using a surgical drill on the order of 1 mm in diameter. The implant's internal receiver, which remains sub-dermal, is fixed to the patient's skull. After implantation and a check of device function, the surgical site is closed. The patient must then wear an external transceiver which attaches by a magnet transcutaneously to the internal receiver.

The implanted electrode arrays come in several forms ranging from straight electrode arrays that follow the lateral wall to pre-curved electrode arrays that follow the mid-scala or hug the inner (modiolar) wall of the ST. In this work, we focus on the PEA as a case study. This selection was based on the under-actuated structure of PEA's which can be indirectly steered during implantation using intelligent control of an embedded stylet.

Intra-cochlear trauma has been a focus of numerous studies[1,7,11,15,27,36,36] with an emphasis on mitigating damage to the intra-cochlear anatomy. Clinical evidence suggests that trauma mitigation is correlated with improved retention of residual hearing.[7] There is also evidence that preserving residual hearing improves speech recognition in complex sound environments.[14] Because of these studies there has been an increased emphasis on the importance of inserting PEA's using "soft" technique in order to avoid intra-cochlear trauma.[1,13]

In 2005, Roland[28] included the measurement of insertion force as an additional quantitative post-operative metric of insertion quality which has subsequently been used by a variety of groups. In 2007, Todd reported insertion forces below 0.05N using PEA's in highly controlled laboratory insertion experiments.[33] Other reported insertion forces have been mostly below 20 mN in magnitude across different types of implants. Such low forces are below the threshold of accurate human perception[3,16] and have presented a need for new tools with embedded force sensing capability to be used. Several works have presented prototypes for automated insertion using force sensing as either single[19,20,31] or multi degree-of-freedom (DoF) devices.[39,40]

Different types of complications can occur during the process of inserting the CI into the cochlea. This work focuses on the tip folding complication. In tip folding cases, the distal tip of the electrode folds over on itself during insertion. This results in some electrode contacts being poorly positioned with respect to the auditory nerve. It also effectively doubles the cross sectional area of the electrode array as it moves through the ST. Tip folding has been discussed in several works

https://doi.org/10.1017/S0263574716000333 Published online by Cambridge University Press

with Briggs addressing it during the development of perimodiolar designs[4,5] and as a consideration in magnetically steerable electrode array prototypes.[8] The rate of tip folding is not well known in clinical practice although is expected to be rare with experienced surgeons. However, for a tool intended to autonomously deploy implants, the clinical risk of folding the implant during insertion requires the presence of safety algorithms that can mitigate the likelihood of inducing trauma.

3. Robotic Insertion of CI Electrodes

The kinematics of robotic PEA insertion and the type of data collected are reviewed in this section with additional details presented in ref. [24, 25]. The insertion of CI electrode arrays into a cochlea phantom model was carried out using a custom-designed robotic-tool while assuming manufacturer-recommended insertion technique. This phantom model was provided by Cochlear Ltd. The choice of the phantom model for the execution of the insertions was motivated by the need to easily observe the behavior of the PEA's during insertion to confirm insertion conditions. In our previous studies, it was observed that insertion forces were generally higher in temporal bones than in the plastic model.[25] However, it was hypothesized that the reason for increased force was due to the uncertainty in determining the correct point to begin advancing off of the stylet. This was tested through the use of a hybrid force/position admittance controller and demonstrated that insertion forces in cadaveric specimens were comparable to the phantom model insertions when the control was capable of correcting the pre-defined start of advancing off the stylet in the insertion trajectory.[26]

It is assumed that access to the cochlea has been created through a mastoidectomy. The entrance to the cochlea is made through either the round window or an anterior–inferior cochleostomy. Regardless of the technique, the point of entry into the cochlea will be denoted as the *insertion point*.

The implant electrode used exclusively in these experiments was the Cochlear *Contour Advance* PEA. This type of implant is actuated through the removal of an embedded metal stylet in the pre-shaped silicone body of the electrode array. When the stylet is completely removed, the PEA is curled so as to maintain close proximity of the modiolar (inner) wall of the cochlea. As the PEA is inserted into the cochlea's ST chamber, the removal of the stylet is coordinated with the insertion progress using a technique called *Advance Off Stylet* (AOS). With this technique, the stylet is not disturbed until approximately 7 mm of the PEA has entered the ST. A small mark on the exterior body of the *Contour Advance* indicates this depth of insertion for the surgeon. To insert the PEA past the 7 mm depth the surgeon holds the stylet fixed and advances the electrode array off the stylet. Figure 3 (A) thru (C) presents a rendering of the AOS technique in a 2D profile of the ST chamber shape. The figure shows the PEA and the ST in an accurate size scale relative to each other. This study included purposely selected and modified prototypes of the *Contour Advance*, with manufacturing defects and malfunctions, aimed to induce or facilitate tip folding events, at rates very significantly higher to any experience reported in clinical practice with this electrode design.

The insertion depth of electrode arrays is often parameterized by either linear depth, q,[20,25,28,31,33,38] or by the insertion angle about the cochlea helix, θ,[1,2,5,9,36] that points to the distal tip of the electrode array. In this work, we present insertion force based on linear depth $q \in [0, L]$ where L is the electrode array length. This representation was chosen because linear depth estimates may be made in real time by the robot controller. Instead of using the absolute insertion depth $q \in [0, L]$ we use a normalized insertion depth $\lambda = \frac{q}{q_{range}}$ because it was observed in ref. [24, 25] that in the final millimeter of electrode insertion the gripper contact with the facial recess may corrupt measurement of purely intra-cochlear reaction force. The constant q_{range} is a fraction of L used to exclude contact of the gripper holding the PEA with the facial recess. By specifying $q_{range} = 14$ mm, we removed contact events from all insertion data and allowed for fair comparison of intra-cochlear forces.

A rendering of the robotic insertion system is shown in Fig. 4. A Stewart/Gough parallel robot ① carries a force sensing and stylet actuation module ② and a gripper holding a PEA ③. The gripper has an attached frame $\{\mathbf{A}\}$ located at a pose $\mathbf{x}$ expressed in the robot's base frame $\{\mathbf{B}\}$. The pose vector $\mathbf{x} \in \mathbb{R}^7$ contains the homogeneous transformation with a three element cartesian translation vector and a unit quaternion.

https://doi.org/10.1017/S0263574716000333 Published online by Cambridge University Press

Fig. 3. *Advance Off Stylet* insertion technique. (a) The PEA is inserted until the distal end reaches the basal turn. (b) Stylet retraction is coordinated with continued insertion into the scala tympani. (c) At full insertion depth the stylet is completely. (d) Normal insertions result in the PEA electrodes being in close contact with the modiolus. (e) Tip-folding results in the distal tip of the PEA bending over itself inside the cochlea.

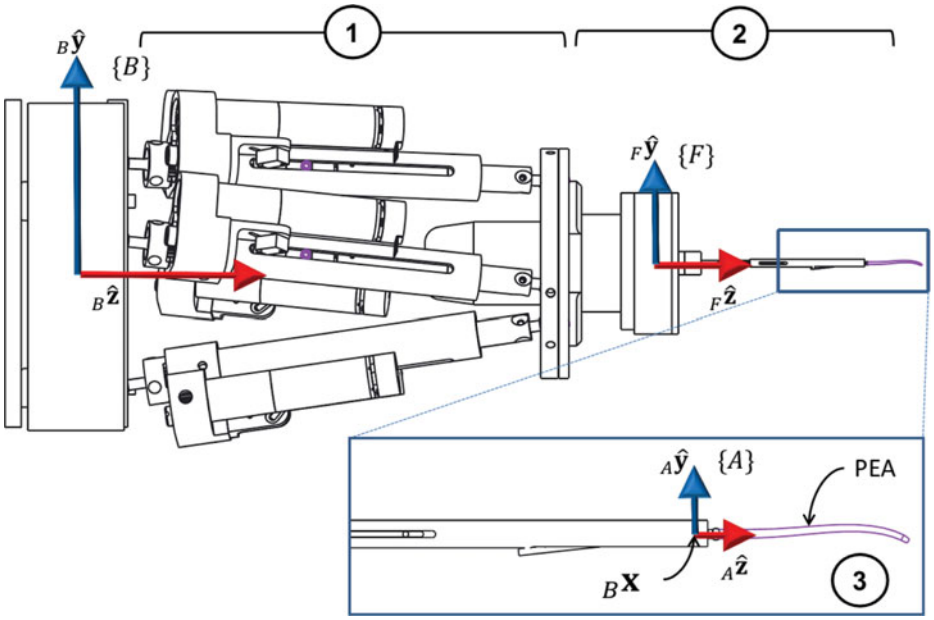

Fig. 4. Robotic insertion system with frame definitions. The gripper frame {**A**} is located at a point **x** in the robot base frame {**B**}. The force sensor measurements are expressed in frame {**F**}. The key components of the system include (1) the six dof Stewart–Gough style robotic manipulator, (2) the gripper module that both holds and actuates the PEA, and (3) the PEA implant.

The insertion trajectory was calculated as a linear interpolation between an initial and final position of the gripper holding the PEA as described in ref. [25]. The pose of the gripper as a function of insertion depth is denoted as $\mathbf{x}(q)$. At the beginning of insertion $q_0 = 0$ and at the end of the insertion $q = q_{max} \geq q_{range}$. The PEA design requires coordinated actuation of the embedded stylet with the magnitude of stylet retraction denoted by the variable $q_s(q)$. Once reaching the proper insertion depth to start AOS (q_{AOS}) the stylet is retracted at the same rate that the PEA advances into the cochlea. In the observer's frame of reference, the PEA will appear to advance off of the stylet. The magnitude of stylet retraction is expressed as:

$$q_s(q) = \begin{cases} 0, & q \leq q_{AOS} \\ q - q_{AOS}, & q > q_{AOS} \end{cases}. \tag{1}$$

https://doi.org/10.1017/S0263574716000333 Published online by Cambridge University Press

Table I. Experimental matrix.

Set	Specimen	Insertion type	Rate (mm/s)	# of trials
1	Phantom	Normal	1	51
2	Phantom	Folding	1	51

4. Experimental Design

The objective of this research was to characterize insertion forces of PEA's and to test methods in which this force information could be used to identify an insertion complication before the insertion completed. The transparent model allowed microscope observation of the PEA's during insertion. Using these observations the data could be classified by the resulting type of insertion. The resulting types of insertions were defined into two groups. Normal insertions correspond to proper placement of the PEA, with electrodes contacting the modiolar wall. Folding insertions were any cases where the tip of the PEA bent back toward the base of the PEA.

Premature disruption of the stylet before insertion can lead to tip folding and although uncommon in clinical execution, intelligent autonomous, or cooperative tools need the ability to determine if their actions are leading to unintended and undesirable outcomes. The set of insertions performed are detailed in Table I. Visual presentations of normal and folding insertions are shown in Fig. 3 (d) and (e), respectively. Tip folding was deliberately induced by using selected research electrodes with manufacturing defects and deploying them prematurely in the phantom model of the cochlea. The purpose of this set up was to achieve as many cases of tip folding as possible (in contrast with real electrode/product behavior in clinical cases).

The phantom model mimics the shape of a left side temporal bone with the mastoidectomy and cochleostomy performed. The cochlea was removed from the model and placed in a new holder to allow a digital microscope to monitor inter and extra-cochlear PEA mechanical behavior. Before proceeding with PEA insertions the cochlea was filled with a 50% glycol solution to mimic lubrication properties of perilymph. Using glycol solution for lubrication has been presented in ref. [28] and validated against other lubrication alternatives in ref. [18]. After preparation, the phantom model was secured within the workspace of the robotic insertion system.

The experimental setup for the insertion of PEA is shown in Fig. 5. The insertion system is a custom made six DoF Stewart/Gough parallel robot rigidly fixed with respect to the phantom first presented in ref. [39]. A gripper module with one dof to actuate the PEA's stylet is mounted on a six axis force/moment transducer (Nano43, *ATI Industrial, Apex, NC*) which is in turn connected to the moving platform of the robot. The controller for the robotic system ran under the xPC Target real time OS from Mathworks.

During each insertion experiment the specimen was fixed in position relative to the robot. Next, the gripper was tele-manipulated to the insertion point $\mathbf{x}(q_{max})$ in the cochlea in order to digitize this point for calculation of the insertion trajectory. The gripper was then retracted to enable loading the PEA. After loading, the electrode tip was guided to the insertion point. Once the PEA was in position, the insertion trajectory was calculated and then executed. Once insertion was completed, the electrode was retracted and the force data exported from the control computer for processing.

Each insertion was executed at a fixed rate (i.e. $\dot{q} = 1$ mm/s) with force measurements sampled at 1000 kHz and processed through a 25 ms moving average filter. The insertion speed was selected based on the range defined in prior works in phantom models.[17,37] The force resolution for the sensor was 4 mN per axis and moment resolution was 0.025 N-mm per axis. The force and moment vector is denoted as a wrench $\mathbf{w} = \left[f_x, f_y, f_z, f_{xx}, f_{yy}, f_{zz}\right]^T$ and presented in the force sensor frame $\{\mathbf{F}\}$ as shown in Fig. 4.

Tip folding cases were generated by actuating (retracting) the stylet by 0.5 mm before the insertion (off the stylet, *AOS*) into the cochlea begins. This simulates improper loading of the PEA into the gripper or other significant disturbances to the distal tip of the PEA or its stylet prior to use. In practice, the PEA should not have its stylet retracted until after the electrode is fully inserted into the ST.

The force component f_z is referred to as the *insertion force*, f_x, f_y are the *lateral forces*, and f_{xx}, f_{yy} are the *lateral moments*. The moment f_{zz} is the twisting moment along the electrode array's

https://doi.org/10.1017/S0263574716000333 Published online by Cambridge University Press

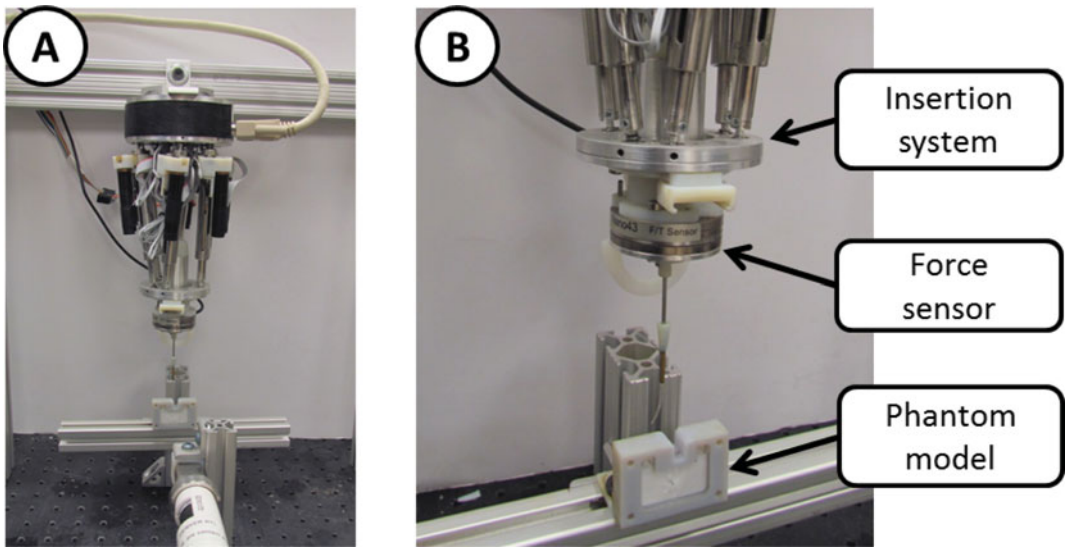

Fig. 5. Experimental setup. {*A*} The insertion system is suspended over the phantom model of the cochlea. Before experiments begin, the robotic system is registered to the phantom model. After loading a PEA into the insertion system, the force sensor is unbiased for the weight of the PEA and the insertion trial would then be executed. Sub-figure {*B*} presents a closer view of the robotic end effector, force sensor and the phantom cochlea model.

long axis and due to the PEA's compliance reaction moments in this direction are too small to be perceptible by the sensor used in this study.

5. Detection of the Onset of Tip Folding

There are several basic clinical objectives that must be fulfilled in the process of detecting tip folding to make the algorithm useful in a realistic setting:

(1) The detection algorithm should not be identifying folding events before initiating AOS since it is not consistent with the conditions required for real folding to occur.
(2) The detection algorithm should identify a folding event as close to the start of AOS as possible to prevent forcing a folded electrode array deeper into the cochlea.
(3) There is increased risk of trauma in removing an implant and inserting a new one so the detection algorithm is biased to reducing false positives. This particular goal is a judgement call we have made as an assumption that will be evaluated in future clinical research studies. Regardless our proposed method is inherently tunable to later adjust the acceptable rates of false positive and negatives based on a larger set of experimental data.

The key weakness with our preliminary classification method[25] was that the entire insertion must be completed before a decision could be made. This is undesirable since the folded PEA will have been forced into the ST thus increasing the risk of trauma. The adjusted approach is to make a continuous estimation of the entire insertion wrench throughout the insertion process.

Our approach for tip folding detection is presented in Fig. 6. A tip folding event is determined by a support vector classifier (SVC); a supervised machine learning algorithm applied to tip folding detection. In ref. [25] the SVC rendered a classification decision *after* the insertion was completed. To detect a folding event earlier, we have added a model predictor which uses experimental measurement distributions with the current measurements in order to produce the necessary feature vector to be used by the SVC.

The wrench data is sampled at a high rate with m total measurements for any given insertion. The indexing subscript k references one measurement or prediction with $1 \leq k \leq m$. All data is expressed in terms of the normalized insertion depth vector $\boldsymbol{\lambda} \in \mathbb{R}^m$ with the use of λ_k indicating the kth step of the insertion. In Fig. 6, a model estimator is used to augment the current component wrench measurement $f_j(\lambda_k)$ with the experimental distribution $\bar{\mathbf{f}}_j(\boldsymbol{\lambda})$ to produce a prediction of the insertion wrench

https://doi.org/10.1017/S0263574716000333 Published online by Cambridge University Press

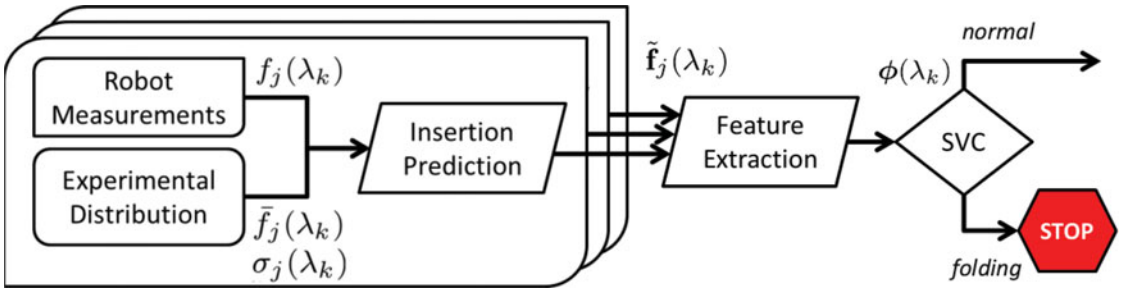

Fig. 6. Tip folding detection process. The subscript j refers to one of the measured wrench components. As a force component measurement f_j is made at depth λ_k, is combined with a known population of normal insertion data with mean $\bar{f}_j$ and variance σ_j to generate an estimate of a likely complete insertion force vector $\tilde{\mathbf{f}}_j$. This estimate is then used to construct a feature vector $\boldsymbol{\phi}$ that is passed to a SVC decision function to decide whether a tip fold has occurred. In the case of tip folding, the robot is instructed to stop further insertion of the PEA into the cochlea.

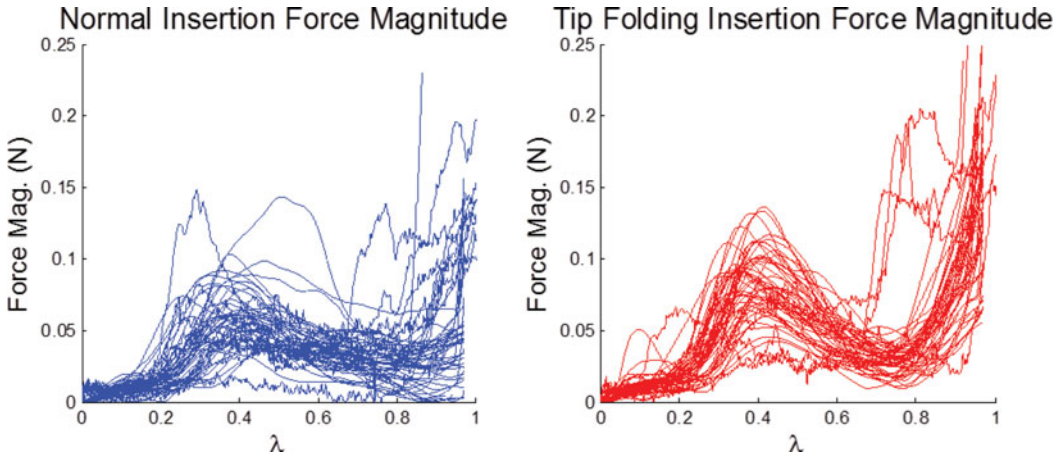

Fig. 7. Insertion force magnitudes based on cases of normal insertion (left) and tip folding insertions (right). Plots are represented in normalized insertion distance λ.

component $\tilde{\mathbf{f}}_j(\boldsymbol{\lambda})$. A subset of the predicted wrench components $\tilde{\mathbf{f}}_j(\boldsymbol{\lambda})$, $j \in [x, y, z, xx, yy, zz]$ are then used to generate a feature vector $\boldsymbol{\phi}(\lambda_k)$ which is used as an input to the SVC.

To generate the predicted wrench components $\tilde{\mathbf{f}}_j(\boldsymbol{\lambda})$ we use an insertion force model $\hat{f}_j(\lambda_k)$. Details of the insertion force model to reduce the amount of numerical data processed are first presented. This is followed by how the insertion force predictions for use with the SVC is generated. Lastly, a modification of the SVC decision function to enable continuous online detection of tip folding throughout the insertion process is presented.

5.1. Insertion force model

Figure 7 depicts average insertion direction forces for normal (blue, left side) and tip folding (red, right side) insertions. The force and moment data collected during the insertion has thousands of samples for each wrench element. Both real time processing and tip folding detection require a numerically compact representation that maintains the measured signal fidelity. The purpose of the force model is to provide this compact representation. It can be seen that one normal insertion appears to terminate early. A large impulse was detected during insertion which caused the system to stop with a shallow insertion. In this case, a final decision must be made by that point in the insertion. Since the insertion was still normal, it was included in the set of experimental data.

Each wrench component is assumed to be a continuous function in the domain of $\lambda \in [0, 1]$. The vector containing the values of the function representing each wrench component is designated by $\mathbf{f}_j(\boldsymbol{\lambda})$ where j is the particular wrench subscript. This vector is the discrete sampling at m points $\boldsymbol{\lambda} = [\lambda_1, \lambda_2, \ldots, \lambda_m]$ of the continuous signal of the F/T sensor during the entire PEA insertion. For

https://doi.org/10.1017/S0263574716000333 Published online by Cambridge University Press

the remainder of this section, the component subscript will be omitted. At a given depth of insertion λ a wrench component $f(\lambda)$ is approximated by a Bernstein polynomial basis representation $\hat{f}(\lambda)$ defined as

$$\hat{f}(\lambda) = \sum_{i=0}^{n} c_i B_i(\lambda), \tag{2}$$

where c_i is a fitting coefficient, n is the fitting order, and $B_i(\lambda)$ is the Bernstein basis computed by the following equation.

$$B_i(\lambda) = \frac{n!}{i!(n-i)!} \left(\lambda^i (1-\lambda)^{n-i}\right), \ \forall i = 0, \ldots, n. \tag{3}$$

The advantages of the Bernstein polynomial basis include orthogonality in the unit domain, its computational efficiency through recursive calculation of the coefficients and its excellent conditioning which reduces the effect of rounding errors in the coefficients.[12] For a given order n and set of m sample points a fitting matrix is constructed

$$\mathbf{B} = \begin{bmatrix} B_1(\lambda_1), & \ldots, & B_n(\lambda_1) \\ \vdots, & \ddots & \vdots \\ B_1(\lambda_m), & \ldots, & B_n(\lambda_m) \end{bmatrix} \in \mathbb{R}^{m \times n+1}. \tag{4}$$

The coefficients vector $\mathbf{c} \in \mathbb{R}^{n+1}$ is determined from the force vector $\mathbf{f}(\boldsymbol{\lambda})$ through the least squares solution

$$\mathbf{c} = \mathbf{B}^{-1}\mathbf{f}(\boldsymbol{\lambda}). \tag{5}$$

Given $\mathbf{c}$, a vector containing the values of the insertion force model (2) is designate by $\hat{\mathbf{f}} \in \mathbb{R}^m$. This vector can be calculated in matrix form as

$$\hat{\mathbf{f}} = \mathbf{B}\,\mathbf{c}. \tag{6}$$

Using the polynomial coefficients will not produce the same vector as the original measurement (i.e. $\hat{\mathbf{f}} \neq \mathbf{f}$) and the root mean square error, ϵ_{RMS}, of this discrepancy is defined as

$$\epsilon_{RMS} = \sqrt{\frac{\left(\hat{\mathbf{f}} - \mathbf{f}\right)^T \left(\hat{\mathbf{f}} - \mathbf{f}\right)}{m}}. \tag{7}$$

The order of the polynomial series was set to $n = 10$ to fit the data with a RMS error comparable to the force sensor noise of $0.004N$ (force) and 0.025 Nmm (moment).

Using this polynomial fitting, the force vector can be resized by changing the number of sample points in $\boldsymbol{\lambda}$. Based on our work,[25] the number of samples per wrench component was set to $m = 25$. From the collection of measured normal insertion data, the average and variance as a function of insertion depth λ are denoted as $\bar{f}_m$ and σ_m respectively. A second subscript denotes the axis of the measurement (i.e. $\bar{f}_{m,z}$ is the average force for the z axis in the force sensor frame $\{\mathbf{F}\}$). Table II presents the fitting coefficients for the averages and variances of the insertion forces and lateral moments from the set of normal insertion data used in the folding detection.

5.2. Estimation of future forces

Our previously trained classification model relied on the entire insertion data set to make a successful classification. The present goal is to make a determination on the detection of tip folding as close to the onset of the event as possible. To do this, a prediction of the future insertion forces, based on what has been currently recorded, is required. The update to this prediction is made at each of the m measured points in the force vector $\mathbf{f} \in \mathbb{R}^m$.

https://doi.org/10.1017/S0263574716000333 Published online by Cambridge University Press

Table II. Insertion force summary.

Coef.	c_0	c_1	c_2	c_3	c_4	c_5	c_6	c_7	c_8	c_9	c_{10}
$\bar{f}_{m,z}$	−0.00368	0.00322	−0.09043	0.27410	−0.66837	0.48569	−0.32705	0.08950	−0.09196	−0.02012	−0.09988
$\sigma_{m,z}$	0.00754	0.00454	−0.07346	0.31662	−0.53801	0.81025	−0.77213	0.51994	−0.15782	0.07319	0.11535
$\bar{f}_{m,xx}$	−0.02584	−0.30809	1.67939	−3.86249	2.56596	3.16762	−4.02440	3.20528	0.00664	−0.12767	−0.41673
$\sigma_{m,xx}$	0.06385	−0.19397	1.17943	−3.78169	9.13224	−5.35123	4.77472	0.43311	1.75574	1.35499	1.47611
$\bar{f}_{m,yy}$	0.01062	−0.10120	0.67325	−2.18398	4.65950	−6.10697	2.50529	−1.68914	−0.12048	−0.69473	−0.19172
$\sigma_{m,yy}$	0.04616	−0.07260	0.39600	−1.43339	4.16891	−3.64368	3.21728	−0.37063	0.87301	0.46814	1.06752

At the kth sample (where $1 \leq k \leq m$) the predicted force vector is denoted by $\tilde{\mathbf{f}}(\lambda_k)$. In the following section, we explain the prediction approach depicted in Fig. 8. At each prediction update the estimated coefficient vector $\tilde{\mathbf{c}}(\lambda_k)$ is determined and then used in Eq. (8) to provide the latest estimation:

$$\tilde{\mathbf{f}}(\lambda_k) = \mathbf{B}(\boldsymbol{\lambda})\,\tilde{\mathbf{c}}(\lambda_k). \tag{8}$$

The coefficients in $\tilde{\mathbf{c}}(\lambda_k)$ converge to $\mathbf{c}$ from Eq. (5) at the final sample ($\tilde{\mathbf{c}}(\lambda_m) = \mathbf{c}$). Our estimation of $\tilde{\mathbf{c}}(\lambda_k)$ is a weighted least squares solution of the form

$$\tilde{\mathbf{c}}(\lambda_k) = \left(\mathbf{B}^T\mathbf{W}_k^{-1}\mathbf{B}\right)^{-1}\mathbf{B}^T\mathbf{W}_k^{-1}\mathbf{g}\,(\lambda_k)\,, \tag{9}$$

where $\mathbf{W}_k$ is the weight matrix and $\mathbf{g}(\lambda_k)$ is the augmented force vector at the kth sample. The vector $\mathbf{g}(\lambda_k)$ is a combination of measurements taken by the robot up to the present position λ_k and an estimated average force $\bar{\mathbf{f}}_k$ for future measurements

$$\mathbf{g}\,(\lambda_k) = \begin{bmatrix}\mathbf{f}_k \\ \bar{\mathbf{f}}_k\end{bmatrix},\ \mathbf{f}_k \triangleq \begin{bmatrix} f\,(\lambda_1) \\ \vdots \\ f\,(\lambda_k)\end{bmatrix},\ \bar{\mathbf{f}}_k \triangleq \begin{bmatrix} \bar{f}\,(\lambda_{k+1}) \\ \vdots \\ \bar{f}\,(\lambda_m)\end{bmatrix}, \tag{10}$$

The weight matrix $\mathbf{W}_k$ ensures that $\tilde{\mathbf{f}}(\lambda_k)$ agrees with the currently known data and passes through the estimated future force averages with weight proportional to an estimated variance. Typically, the best weight matrix would be the covariance matrix of the data set[32] but this is unknown *a-priori* in practice. Instead, the m measurements are considered independent Gaussian distributions with a known variance $\sigma(\lambda)$. The measured force data also has a degree of uncertainty based on sensor accuracy that is parameterized by β. The weighting matrix is thus diagonal and of the form

$$\mathbf{W}_k = \begin{bmatrix} \frac{1}{\beta}\mathbf{I}_{[k\times k]} & \mathbf{0}_{[m-k\times m-k]} \\ \mathbf{0}_{[m-k\times m-k]} & \boldsymbol{\Sigma}_k^{-1}\end{bmatrix}, \tag{11}$$

given that

$$\boldsymbol{\Sigma}_k = \begin{bmatrix} \sigma_m^2(\lambda_{k+1}) & \dots & 0 \\ \vdots & \ddots & \vdots \\ 0 & \dots & \sigma_m^2(\lambda_m)\end{bmatrix} \in \mathbb{R}^{m-k\times m-k}. \tag{12}$$

When constructing the augmented force vector $\mathbf{g}(\lambda_k)$ the most naive future force input would be to use the previously measured averages and variance. In this case, $\bar{f}(\lambda_k) = \bar{f}_m(\lambda_k)$ and $\sigma(\lambda_k) = \sigma_m(\lambda_k)$. This method will cause the prediction to quickly match the experimental average and does not take into account the current magnitude of the insertion forces nor the rate at which they are currently changing. To improve the prediction of $\bar{f}(\lambda)$ and $\sigma(\lambda)$, the average force distribution $\bar{f}_m(\lambda_k)$ and $\sigma_m(\lambda_k)$ are combined with an extrapolated distribution $\bar{f}_e(\lambda_k)$ and $\sigma_e(\lambda_k)$. The two distributions are combined using the method described in ref. [6] such that:

$$\bar{f}(\lambda_j) = \frac{\bar{f}_m(\lambda_j)\sigma_e^2(\lambda_j) + \bar{f}_e(\lambda_j)\sigma_m^2(\lambda_j)}{\sigma_e^2(\lambda_j) + \sigma_m^2(\lambda_j)}, \tag{13}$$

$$\sigma^2(\lambda_j) = \frac{\sigma_e^2(\lambda_j)\sigma_m^2(\lambda_j)}{\sigma_e^2(\lambda_j) + \sigma_m^2(\lambda_j)}. \tag{14}$$

The extrapolated distribution is a first order approximation based on the current force measurement $f(\lambda_k)$ and the measured rate of change of insertion force $f'(\lambda_k) = \frac{df}{d\lambda}$ and its standard deviation as $\sigma'(\lambda_k)$. The extrapolation is first order and starting at the current sample k, the distance in normalized

https://doi.org/10.1017/S0263574716000333 Published online by Cambridge University Press

insertion space to the jth predicted sample is defined as

$$\Delta\lambda_{k,j} = \lambda_j - \lambda_k \;\; \forall k \leq j \leq m. \tag{15}$$

This means that the average extrapolated force has mean $\bar{f}_e$ and is estimated by starting at the current measurement $f(\lambda_k)$ and linearly extrapolating based on the fixed rate $\bar{f}'$ such that

$$\bar{f}_e(\lambda_j) = f(\lambda_k) + \Delta\lambda_{k,j}\, \bar{f}'(\lambda_k) \quad \forall k \leq j \leq m. \tag{16}$$

We assume a linear propagation of the uncertainty distribution with insertion depth. The uncertainty grows proportionally to σ' and the distance travelled $\Delta\lambda_{k,j}$. The extrapolated distribution standard deviation σ_e equal to:

$$\sigma_e(\lambda_j) = \Delta\lambda_{k,j}\, \sigma_d(\lambda_k)\; \forall k \leq j \leq m. \tag{17}$$

This update procedure generates the elements in $\bar{\mathbf{f}}$ from Eq. (10) and the variance matrix $\mathbf{\Sigma}_k$ from Eq. (12). The steps in the predictive calculation are reviewed in Algorithm 1. After generating predictions for the wrench components using Eq. (8) the data is used in the trained classifier to determine if a folding event has begun.

Algorithm 1 Generation of Estimated Force

Require: $\bar{\mathbf{f}}_m, \bar{\sigma}_m, \bar{\mathbf{f}}'_m, \bar{\sigma}'_m$
  for $j = k, \ldots, m$ **do**
    $\Delta\lambda_{k,j}$ from Eq. (15)
    Calculate $\bar{f}_e(\Delta\lambda_{k,j})$ from Eq. (16)
    Calculate $\sigma_e(\Delta\lambda_{k,j})$ from Eq. (17)
  end for
  Calculate $\bar{\mathbf{f}}$ from Eq. (13)
  Calculate $\boldsymbol{\sigma}$ from Eq. (14)
  Construct $\mathbf{g}(\lambda_k)$ from Eq. (10)
  Calculate $\tilde{\mathbf{c}}(\lambda_k)$ from Eq. (9)
  Calculate $\tilde{\mathbf{f}}(\lambda_k)$ from Eq. (8) **return** $\tilde{\mathbf{f}}(\lambda_k)$

Figure 8 shows how the information is combined to form a prediction for insertion force at $\lambda_k = 0.4$. The current point in the insertion process for the shown prediction is designated by a large dot. The average insertion force for a prior sample set of normal insertions is shown as a dashed line. The final insertion force for this particular insertion is shown in the fine solid line. A thick solid line is used to show the predicted force.

5.3. Tip folding classification

To address the separation of normal and tip folding insertion data our previous work[25] used a SVC machine learning algorithm which will be reviewed here.

SVC's can be used to address a variety of problems and a brief review of the SVC algorthm is provided here with greater detail provided in ref. [29, 30]. Our problem is a binary classification task to which the SVC is well suited. In the binary classification problem, a collection of N data sets are classified by the binary vector $f(\mathbf{v}) \in \mathbb{R}^N$ with values of -1 or 1. Each data set is defined by a feature space $\mathbf{v} \in \mathbb{R}^d$ whose values represent the pertinent attributes of that set. The SVC algorithm searches for a hyperplane defined by a vector of weight coefficients $\mathbf{w} \in \mathbb{R}^d$ and a scalar bias b which classifies any data set by the decision function

$$h(\mathbf{v}) = \operatorname{sgn}((\mathbf{w} \cdot \mathbf{v}) + b) \in [-1, 1]. \tag{18}$$

This decision function is inherently linear but the feature space may be mapped into higher dimensions through a kernel function $k\langle \mathbf{v}, \mathbf{v}_i \rangle$. The kernel function relies on a set of feature vectors $\mathbf{v}_i$ taken from a set of training data and each weighted by a coefficient α_i which are collectively called the *support*

https://doi.org/10.1017/S0263574716000333 Published online by Cambridge University Press

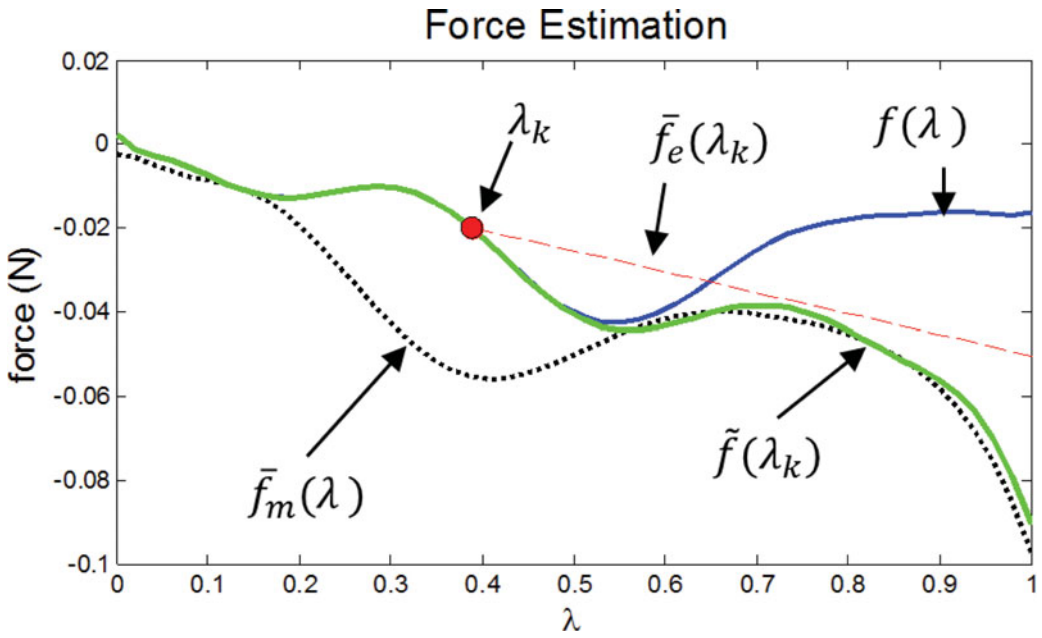

Fig. 8. Example of force prediction. The dashed line is the measured force average $\bar{f}_m(\lambda)$ from prior data. The thin solid line is the true final measurement $f(\lambda)$ for this insertion. The dot represents the current point of the insertion λ_k where the prediction is made. A linearly extrapolation $\bar{f}_e(\lambda_k)$ from the current measurement $f(\lambda_k)$ is made based on the average rate of change $\bar{f}'_m(\lambda_k)$. The thick solid line indicates the final prediction $\tilde{f}(\lambda_k)$ based on a combination of $\bar{f}_m(\lambda_k)$ and $\bar{f}_e(\lambda_k)$.

vectors. The new decision function is written as

$$h(\mathbf{v}) = \sum_{i=1}^{l} \alpha_i k\langle \mathbf{v}_i, \mathbf{v}\rangle + b. \tag{19}$$

The kernel functions used in SVC's are varied but the four most common kernels are the linear, polynomial, radial basis, and sigmoid. Our previous investigation,[25] looked at several combinations of feature spaces and kernel functions. It was determined that a linear kernel with a descretized sampling of insertion direction force and the orthogonal moment components (f_z,f_{xx}, and f_{yy}) had the highest classification accuracy at approximately 90%. The linear kernel defined as

$$k\langle \mathbf{v}_i, \mathbf{v}\rangle_{linear} = \mathbf{v}_i^T \mathbf{v}. \tag{20}$$

The feature space was 75 elements which required the completed insertion before a classification could be made. The vector $\boldsymbol{\lambda}$ is rescaled to $m = 25$ with $\lambda_m = 1$. We propose that the predictive model detailed in the previous section can be used at the kth sample measurement to generate a new feature vector

$$\tilde{\mathbf{v}}(\lambda_k) = \left[\tilde{\mathbf{f}}_{z,k}^T, \tilde{\mathbf{f}}_{xx,k}^T, \tilde{\mathbf{f}}_{yy,k}^T\right]^T \in \mathbb{R}^{d=3m=75}, \tag{21}$$

where $\tilde{\mathbf{f}}_{z,k}$, $\tilde{\mathbf{f}}_{xx,k}$ and $\tilde{\mathbf{f}}_{yy,k}$ are the estimated future insertion force and lateral moments with the frame indices referring to frame $\{F\}$ in Fig. 4.

SVM classifiers can be sensitive to scaling differences between the various features so preconditioning is applied before training the classifier. The vector $\mathbf{o} \in \mathbb{R}^m$ is an offset vector with each element equal to the mean of the same element in the collection of feature vectors used in training the SVM. The matrix $\mathbf{S} \in \mathbb{R}^{m\times m}$ is a diagonal matrix with the diagonal elements equal to the standard deviation of the corresponding feature in the training data. A new preconditioned feature

https://doi.org/10.1017/S0263574716000333 Published online by Cambridge University Press

vector $\boldsymbol{\phi}$ is then defined as:

$$\boldsymbol{\phi}(\lambda_k) = \mathbf{S}^{-1}\left(\tilde{\mathbf{v}}(\lambda_k) - \mathbf{o}\right), \tag{22}$$

which is substituted into Eq. (19) in place of $\mathbf{v}_i$ and results in the decision function:

$$h(\boldsymbol{\phi}) = \sum_{i=1}^{l} \alpha_i k\langle \boldsymbol{\phi}_i, \boldsymbol{\phi}(\lambda_k)\rangle_{linear} + b. \tag{23}$$

This scaling method lets the SVC algorithm find a best fit separation hyperplane where each feature has zero mean and has a variance of unity.

5.4. Folding onset detection

In addition to its high accuracy in our preliminary work, the major advantage of the linear kernel is that prediction error can be linearly propagated through the decision function (23). The estimated feature vector can then be written as

$$\tilde{\mathbf{v}}(\lambda_k) = \mathbf{v} + \boldsymbol{\epsilon}(\lambda_k), \tag{24}$$

where $\boldsymbol{\epsilon}(\lambda_k)$ is the error in the prediction estimation at step k. Substituting Eq. (24) into Eq. (22) and Eq. (23) using a linear kernel and differentiating with respect to $\boldsymbol{\epsilon}$ yields:

$$\frac{dh}{d\boldsymbol{\epsilon}} = \sum_{i=1}^{l} \alpha_i \mathbf{S}^{-1}\mathbf{v}_i. \tag{25}$$

Individual elements of the vector $\boldsymbol{\epsilon}(\lambda_k)$ have their ith index denoted as $\epsilon_i(\lambda_k)$. We assume that only samples estimated beyond the current measurement have a significant effect on the decision function and therefore $\epsilon_i(\lambda_k) = 0,\ \forall\, i \leq k$. Since errors are not considered up to the kth measurement, two auxilary vectors $\mathbf{a}_k$ and $\mathbf{b}_k$ are defined as

$$\begin{aligned} \mathbf{a}_i(\lambda_k) &= \left[v_{i,k+1}, \ldots, v_{i,m}\right]^T \in \mathbb{R}^{m-k} \\ \mathbf{b}(\lambda_k) &= \left[\epsilon_{k+1}, \ldots, \epsilon_m\right]^T \in \mathbb{R}^{m-k} \end{aligned}, \tag{26}$$

which are substituted into Eq. (25), replacing $\tilde{\mathbf{v}}(\lambda_i)$ and $\boldsymbol{\epsilon}$ respectively without loss of information.

$$\frac{dh}{d\mathbf{b}(\lambda_k)} = \sum_{i=k}^{l} \alpha_i \mathbf{S}^{-1}\mathbf{a}_i(\lambda_k) = \mathbf{z}(\lambda_k). \tag{27}$$

The effect of $\mathbf{b}(\lambda_k)$ on the deviation of the decision function (parameterized as δh) is not known precisely but can be bounded using the Cauchy–Schwarz inequality

$$\delta h(\lambda_k) \leq \|\mathbf{z}(\lambda_k)\|\|\mathbf{b}_k\|. \tag{28}$$

The value of $\mathbf{z}(\lambda_k)$ is easily calculated from the trained support vectors and $\|\mathbf{b}_k\|$ is estimated from evaluating the prediction model error as a function of λ as shown from the set of data used in training the SVC. The bound on the uncertainty from Eq. (28) is highly conservative and can be tuned by introducing a scalar constant $\rho \in [0, 1]$. The final real time classification of folding event then becomes

$$g(\lambda_k) = \begin{cases} -1 & \text{if } h(\tilde{\mathbf{v}}_k) + \rho\|\mathbf{z}(\lambda_k)\|\|\mathbf{b}(\lambda_k)\| \leq 0 \\ 1 & \text{otherwise} \end{cases}. \tag{29}$$

Since a negative value in Eq. (29) indicates a tip folding event, this approach is biased toward false negative as stated previously in our list of clinical objectives.

https://doi.org/10.1017/S0263574716000333 Published online by Cambridge University Press

Table III. Classification errors.

ρ	0	0.25	0.5	0.75	1
False positives (%)	12	6	6	5	5
False negatives (%)	2	4	4	4	4
Combined accuracy (%)	81	87	87	88	88

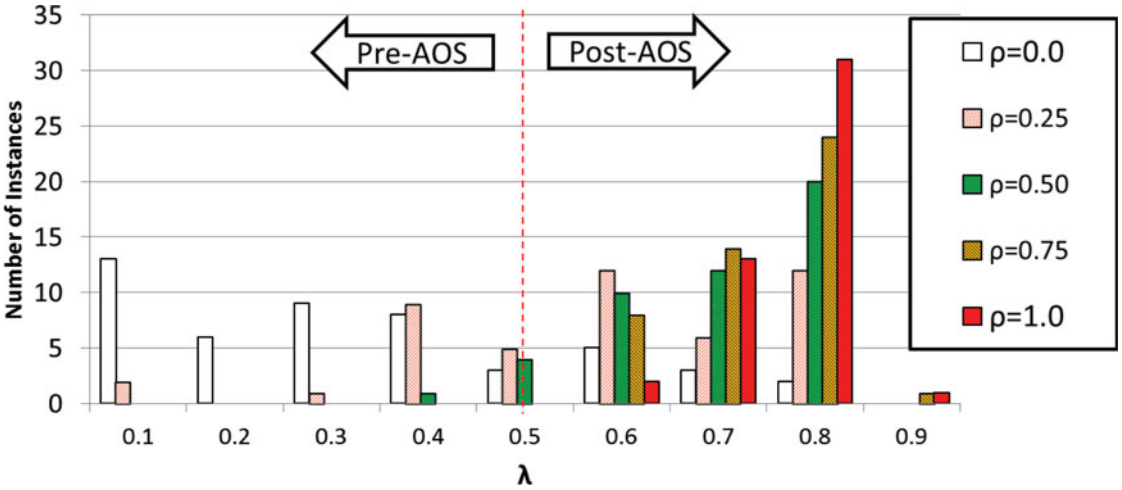

Fig. 9. Tip folding onset detection. The grouped histogram shows the number of detected folding insertions at normalized insertion points from 0 to 1 in 0.1 increments. The dashed vertical line is the point where AOS begins. No folding events should be reported before this point. Five values of ρ used in the decision function are shown at each histogram group. The higher the value of ρ the more conservative the detection algorithm becomes in declaring a folding event.

6. Results and Discussion

The SVC training used a randomized set of 40 insertions using a ten-fold sampling process as discussed in ref. [25]. The training result from our prior work was used with an additional 20 insertion experiments added for testing the classifier. Our objective was to quantify the overall detection accuracy and determine at which point in the insertion process the tip folding could be detected from the set of purposely induced folding events.

Classification was treated as a one way process, once the algorithm returned a tip-folding event the insertion could not be classified as normal. A *false positive* is defined as identifying a normal insertion as a tip folding event. A *false negative* is defined as a tip folding insertion that the SVC identifies as normal. The *combined accuracy* is defined as the ratio of the correctly identified normal and folding insertions compared to the total number of insertions.

The primary goal of the predictive model is to identify tip folding events as soon as possible. Figure 9 presents a histogram of onset detection with the insertion domain divided into 10 equal bins. Five values of ρ are shown to see the effect of the uncertainty margin on the point of onset detection. The vertical dashed line represents the point of initiation for *AOS* technique. Due to the mechanics of tip folding, the detection algorithm should not detect folding event until after *AOS* begins.

As the uncertainty margin increases as ρ approaches 1, the tip-folding detection is delayed as the SVC decision function must have a stronger degree of confidence to declare a folding event early. With higher margins ($\rho > 0.5$) the accidental declaration of a folding event before AOS is eliminated. With no margin applied, there are cases of accidental folding detection early in the insertion process.

Table III shows the number of false positives and negatives for different values of ρ. The 25 insertions used in the SVC were removed from the processing of the results. Adjusting the uncertainty margin has little effect on the number of false negatives, with the most conservative bound ($\rho = 1$) allowing one additional tip folding event to be missed. Without the uncertainty margin ($\rho = 0$), the number of false positives increases drastically. Based on the results shown in Table III we have selected $\rho = 0.75$ for our insertion system.

https://doi.org/10.1017/S0263574716000333 Published online by Cambridge University Press

As expected, from Table III we see that classification accuracy reaches a comparable value of 88% to our preliminary result using full insertion depth data.

6.1. Discussion

The results of our classification method have demonstrated that force and trajectory data can be used to infer intra-cochlear tip folding with a reasonable degree of success. We have made several simplifications in the design of this classification method that must be addressed to provide the proper context to our results. In this work, we have restricted our experiments to a single nominal cochlea geometry while there is some variation in practice between different cochlea in regards to cross sectional area of the scala chambers and the contour of the helical spiral. In live patients, this geometric data can be retrieved through pre-operative imaging and segmentation as demonstrated by Noble *et al.*[22]

We plan to expand our feature space in future work to include geometric parameterization of the cochlea. For example, Cohen[9] has proposed modeling locations in the cochlea spiral through a parametric equation with only a few independent variables. Such a model is well suited to SVM classification since it does not add a large number of dimensions to the feature space. Our existing results exist in a sub-space of this larger feature set and can be incorporated into new training data where cochlea geometry varies. The inclusion of geometric variability will require a larger set of experiments but so long as the geometric data can be measured it does not represent a significant impediment to our method. What will be required of this study is the determination of a compact and complete set of features to describe the geometry of the cochlea.

As discussed in the introduction, we have focused on tip folding detection in this work but mentioned two other insertion failure modes. The first is extra-cochlear buckling of the electrode array during insertion. This failure mode typically occurs early in the insertion process where the distal tip of the electrode array is not well supported. The forces and moments required to deform the implant are significantly higher than the magnitudes we report here (greater than 200 mN) and our system stops insertion for such high loads. Also, visual observation may be a better metric for extra-cochlear buckling since the electrode is still visible to the surgeon/robotic system.

A second insertion complication where this type of force based identification is useful is in identifying scala crossing during insertion. This is when the tip of the electrode array punctures the basilar membrane and moves from the ST to SV. It is highly likely that such a puncture can be detected through force measurements and may alter the results of our classification method. This motivates a future research direction to examine the insertion forces observed during scala crossings. Since this complication requires the full cochlea, it will be a clinically focused study in fresh cadaveric specimens.

7. Conclusion

The goal of this work was to expand the use of real time force sensing in the CI robotic insertion to provide a means of detecting complications in the insertion process. Thus far in the literature, robotics applied in the CI procedure have not used real time sensing in this capacity. Tip folding of PEA's was induced by using selected research electrodes with manufacturing defects and improper manipulation, in a phantom (plastic) model of the cochlea, and used as a case study to demonstrate that intra-cochlear phenomenon could be perceived through extra-cochlear measurements. For our work the tip folding event was deliberately induced on defective research PEA's to replicate the phenomenon. We plan to expand this machine learning method to detect other adverse events such as scala crossing in the future. The Bernstein polynomial basis presented here also allows us to report insertion force measurements in a compact and accurate way that can allow the measurements to be more accurately disseminated in the literature. Combined with our prior work in force admittance control to CI insertion this work continues to build a force-based CI insertion control algorithm with application in laboratory electrode evaluation and future clinical deployment.

Acknowledgements

This work has been funded by Cochlear Ltd. (Sydney, Australia) and we would like to thank Cochlear for support during this research.

Supplementary material

To view supplementary material for this article, please visit http://dx.doi.org/10.1017/S0263574716000333.

References

1. O. Adunka, W. Gstoettner, M. Hambek, M. H. Unkelbach, A. Radeloff and J. Kiefer, "Preservation of basal inner ear structures in cochlear implantation," *ORL; J. Oto-Rhino-Laryngology Relat. Specialties* **66**(6), 306–12 (2004a).
2. O. Adunka, J. Kiefer, M. Unkelbach and T. Lehnert, "Development and evaluation of an improved cochlear implant electrode design for electric acoustic stimulation," *The Laryngoscope* **114** (July), 1237–1241 (2004b).
3. G. Baud-bovy and E. Gatti, "Hand-held object force direction identification," *Lecture Notes Comput. Sci.* **6192**, 231–236 (2010).
4. R. J. Briggs, M. Tykocinski, E. Saunders, W. Hellier, M. Dahm, B. Pyman and G. M. Clark, "Surgical implications of perimodiolar cochlear implant electrode design: Avoiding intracochlear damage and scala vestibuli insertion," *Cochlear Implants Int.* **2**(2), 135–49 (2001).
5. R. J. S. Briggs, M. Tykocinski, R. Lazsig, A. Aschendorff, T. Lenarz, T. Stöver, B. Fraysse, M. Marx, J. T. Roland, P. S. Roland., C. G. Wright, B. J. Gantz, J. F. Patrick and F. Risi, "Development and evaluation of the modiolar research array–multi-centre collaborative study in human temporal bones," *Cochlear Implants Int.* **12**(3), 129–39 (2011).
6. P. A. Bromiley, "Products and convolutions of Gaussian distributions," Tech. rep., Medical School, Univ. Manchester, Manchester, UK, Tech. Rep 3, Manchester, UK (2003).
7. M. L. Carlson, C. L. W. Driscoll, R. H. Gifford, G. J. Service, N. M. Tombers, B. J. Hughes-Borst, B. a. Neff and C. W. Beatty, "Implications of minimizing trauma during conventional cochlear implantation," *Otology Neurotology* **32**(6), 962–8 (2011).
8. J. R. Clark, Toward Improved Cochlear Implant Insertion Using Magnetic Guidance. Masters' Thesis, University of Utah (2011).
9. L. T. Cohen, J. Xu, S. A. Xu and G. M. Clark, "Improved and simplified methods for specifying positions of the electrode bands of a cochlear implant array," *Am. J. Otology* **17**(6), 859–65 (1996).
10. M. Cosetti and J. T. Roland Jr, "Cochlear implant electrode insertion," *Operative Tech. Otolaryngology Head Neck Surg.* **21**(4), 223–232 (2010).
11. A. Eshraghi, N. Yang and T. Balkany, "Comparative study of cochlear damage with three perimodiolar electride designs," *Laryngeoscope* **113**, 415–419 (2003).
12. R. T. Farouki and T. N. T. Goodman, "On the optimal stability of the Bernstein basis," *Math. Comput.* **65**(216), 1553–1567 (1996).
13. C. C. Finley, T. A. Holden, L. K. Holden, B. R. Whiting, R. A. Chole, G. J. Neely, T. E. Hullar and M. W. Skinner, "Role of electrode placement as a contributor to variability in cochlear implant outcomes," *Otology Neurotology* **29**(7), 920–8 (2008).
14. R. H. Gifford, M. F. Dorman, H. Skarzynski, A. Lorens, M. Polak, C. L. W. Driscoll, P. Roland and C. A. Buchman, "Cochlear implantation with hearing preservation yields significant benefit for speech recognition in complex listening environments," *Ear Hearing* **34**(4), 413–25 (2013).
15. H. N. Ibrahim, S. Helbig, D. Bossard and E. Truy, "Surgical trauma after sequential insertion of intracochlear catheters and electrode arrays (a histologic study)," *Otology Neurotology* **32**(9), 1448–54 (2011).
16. H. H. King, R. Donlin and B. Hannaford, "Perceptual thresholds for single vs. multi-finger haptic interaction," *Proceedings of the IEEE Haptics Symposium,* IEEE, Waltham, MA USA (2010) pp. 95–99.
17. G. Kontorinis, T. Lenarz, T. Stöver and G. Paasche, "Impact of the insertion speed of cochlear implant electrodes on the insertion forces," *Otology Neurotology* **32**(4), 565–70, (2011).
18. G. Kontorinis, G. Paasche, T. Lenarz and T. Stöver, "The effect of different lubricants on cochlear implant electrode insertion forces," *Otology Neurotology* **32**(7), 1050–6 (2011b).
19. O. Majdani, D. Schurzig, A. Hussong, T. Rau, J. Wittkopf, T. Lenarz and R. F. Labadie, "Force measurement of insertion of cochlear implant electrode arrays in vitro: Comparison of surgeon to automated insertion tool," *Acta Oto-Laryngologica* **130**(1), 31–6 (2010).
20. M. Miroir, Y. Nguyen, G. Kazmitcheff, E. Ferrary, O. Sterkers, A. B. Grayeli, "Friction force measurement during cochlear implant insertion: Application to a force-controlled insertion tool design," *Otology Neurotology* **33**(6), 1092–100 (2012).
21. NIH Medical Arts, accessed 2011. http://www.medarts.nih.gov/.
22. J. H. Noble, R. F. Labadie, O. Majdani and B. M. Dawant, "Automatic segmentation of intracochlear anatomy in conventional CT," *IEEE Trans. Bio-Med. Eng.* **58**(9), 2625–32 (2011).
23. J. Pile, M. Y. Cheung, J. Zhang and N. Simaan, "Algorithms and design Considerations for Robot Assisted Insertion of Perimodiolar Electrode Arrays," *IEEE International Conference on Robotics and Automation (ICRA'2011),* Shanghai, China (2011) pp. 2898–2904.
24. J. Pile, S. Member and N. Simaan, "Modeling, design, and evaluation of a parallel robot for cochlear implant surgery," *IEEE/ASME Trans. Mechatronics* **19**(6), 1746–1755 (2014).

25. J. Pile and N. Simaan, "Characterization of Friction and Speed effects and Methods for Detection of Cochlear Implant Electrode Tip Fold-Over," *Proceedings of the IEEE International Conference on Robotics and Automation,* IEEE, Karlsruhe, Germany (May 2013) pp. 4409–4414.
26. J. Pile, G. B. Wanna and N. Simaan, "Force-Based Flexible Path Plans for Robotic Electrode Insertion," *Proceedings of the IEEE International Conference on Robotics and Automation,* IEEE, Hong Kong (2014b) pp. 297–303.
27. P. Rohani, J. Pile, L. a. Kahrs, R. Balachandran, G. S. Blachon, N. Simaan and R. F. Labadie, "Forces and trauma associated with minimally invasive image-guided cochlear implantation," *Otolaryngology* **150**(4), 638–45 (2014).
28. J. T. Roland, "A model for cochlear implant electrode insertion and force evaluation: Results with a new electrode design and insertion technique," *Laryngoscope* **115**(8), 1325–39 (2005).
29. B. Scholkopf, C. Burges and A. Smola (Eds.), *Advances in Kernel Methods: Support Vector Learning* (MIT Press, Cambridge, UK, 1999).
30. B. Schölkopf and A. Smola, "New support vector algorithms," *Neural Comput.* **1245**(x), 1207–1245 (2000).
31. D. Schurzig, R. J. Webster, M. S. Dietrich and R. F. Labadie, "Force of cochlear implant electrode insertion performed by a robotic insertion tool: Comparison of traditional versus Advance Off-Stylet techniques," *Otology Neurotology* **31**(8), 1207–10 (2010).
32. G. Strang, *Computational Science and Engineering* (Wellesley Cambridge Press, Wellesley, MA USA, 2007).
33. C. A. Todd, F. Naghdy and M. J. Svehla, "Force application during cochlear implant insertion: An analysis for improvement of surgeon technique," *IEEE Trans. Bio-Med. Eng.* **54**(7), 1247–55 (2007).
34. G. B. Wanna, J. H. Noble, M. L. Carlson, R. H. Gifford, M. S. Dietrich, D. S. Haynes, B. M. Dawant and R. F. Labadie, "Impact of electrode design and surgical approach on scalar location and cochlear implant outcomes," *Laryngoscope* **124**(Suppl6), 1–7 (2014).
35. G. B. Wanna, J. H. Noble, T. R. McRackan, B. M. Dawant, M. S. Dietrich, L. D. Watkins, A. Rivas, T. A. Schuman and R. F. Labadie, "Assessment of electrode placement and audiological outcomes in bilateral cochlear implantation," *Otology Neurotology* **32**(3), 428–32 (2011).
36. P. Wardrop, D. Whinney, S. J. Rebscher, W. Luxford and P. Leake, "A temporal bone study of insertion trauma and intracochlear position of cochlear implant electrodes. II: Comparison of Spiral Clarion and HiFocus II electrodes," *Hearing Res.* **203**(1-2), 68–79 (2005).
37. J. Zhang, S. Bhattacharyya and N. Simaan, "Model and Parameter Identification of Friction During Robotic Insertion of Cochlear-Implant Electrode Arrays," *Proceedings of the IEEE International Conference on Robotics and Automation* (Kobe, Japan, 2009a) 3859–3864.
38. J. Zhang, J. T. Roland, S. Manolidis and N. Simaan, "Optimal path planning for robotic insertion of steerable electrode arrays in cochlear implant surgery," *J. Med. Devices* **3**(1), 011001 (2009b).
39. J. Zhang, W. Wei, J. Ding, J. T. Roland, S. Manolidis and N. Simaan, "Inroads toward robot-assisted cochlear implant surgery using steerable electrode arrays," *Otology Neurotology* **1**, 1199–1206 (2010).
40. J. Zhang, K. Xu, N. Simaan and S. Manolidis, "A Pilot Study of Robot-Assisted Cochlear Implant Surgery Using Steerable Electrode Arrays," *Medical Image Computing and Computer-Assisted Intervention : MICCAI ... International Conference on Medical Image Computing and Computer-Assisted Intervention* vol. 9 (Pt 1) (Copenhagen, Denmark, Jan. 2006) 33–40.